# Samples of Stars Beyond the Solar System: Silicate Grains in Interplanetary Dust

**Scott Messenger,[1] Lindsay P. Keller,[2] Frank J. Stadermann,[1] Robert M. Walker,[1] Ernst Zinner[1]**

We have identified six circumstellar silicate grains within interplanetary dust particles (IDPs). Their extrasolar origins are demonstrated by their extremely anomalous oxygen isotopic compositions. Three $^{17}O$-rich grains appear to originate from red giant or asymptotic giant branch stars. One $^{16}O$-rich grain may be from a metal-poor star. Two $^{16}O$-poor grains have unknown stellar sources. One of the grains is forsterite, and two are amorphous silicate "GEMS" (glass with embedded metal and sulfides), which is consistent with astronomical identifications of crystalline and amorphous silicates in the outflows of evolved stars. These observations suggest cometary origins of these IDPs and underscore the perplexing absence of silicates among circumstellar dust grains from meteorites.

For more than two decades, NASA has collected interplanetary dust particles (IDPs) in the stratosphere (*1*). These particles are fragments of comets and asteroids; however, the sources of specific IDPs are uncertain (*2*). Most collected IDPs range in size from 5 to 50 μm and are frequently comprised of complex assemblages of 100- to 500-nm crystalline and amorphous grains bound together by carbonaceous material. Anhydrous IDPs' parent bodies have not experienced the hydrothermal alteration evident in meteorites, and many contain well-preserved molecular cloud material (*3*–*5*).

Several types of circumstellar dust grains (stardust) have been extracted from meteorites, including nanodiamonds, silicon carbide, graphite, silicon nitride, corundum, hibonite, and spinel (*6*, *7*). However, despite their cosmically high abundance, no circumstellar silicates have been found in meteorites (*8*, *9*). One possibility is that silicates were more prone to destruction by parent-body or nebular processing in the early solar system. It has been proposed that anhydrous IDPs have preserved circumstellar silicates (*10*–*13*). Although previously measured O, Si, and Mg isotopic ratios of IDPs have fallen within the range of solar system materials, those measurements were limited to >1 μm spatial resolution (*14*–*18*).

**Oxygen isotopic imaging of IDPs.** We performed oxygen isotopic imaging of fragments from nine anhydrous cluster IDPs with a NanoSIMS ion microprobe (*19*). The NanoSIMS enables isotopic measurements at a spatial scale of 100 nm, with unprecedented sensitivity. Three types of samples were analyzed: 5- to 10-μm fragments pressed into Au substrates, 70-nm thin sections mounted on transmission electron microscopy (TEM) grids, and 70-nm sections deposited directly onto Au. Five sections were analyzed by TEM before ion probe analysis to compare the mineralogy with the isotopic compositions of 113 grains. One IDP was sectioned for TEM analysis after ion imaging (*20*). Oxygen isotopic ratios were determined for an additional 919 grains of undetermined mineralogy (*21*). Simultaneously acquired $O^-$, $Si^-$, and $MgO^-$ images served to distinguish oxides from silicates. Because previous studies have found that the bulk O isotopic compositions of IDPs are solar within about 5% (*14*, *18*, *22*), we used the subgrains in each IDP as isotopic standards (*23*).

Most of the 1031 grains have solar O isotopic ratios (Fig. 1). However, six of the grains have O isotopic ratios that are well outside the range of solar system materials and are thus probable stellar condensates (Table 1). These grains are distinguished in the O isotopic images from the surrounding isotopically solar IDP matrices (Fig. 2).

The O isotopic ratios of the circumstellar silicates are compared to those previously reported for circumstellar oxide grains extracted from meteorites (Fig. 3). These grains fall within four isotopic groups (*24*) that reflect differences in

[1]Laboratory for Space Sciences and Physics Department, Washington University, St. Louis, MO 63130, USA. [2]Mail Code SR, NASA Johnson Space Center, Houston, TX 77058, USA.

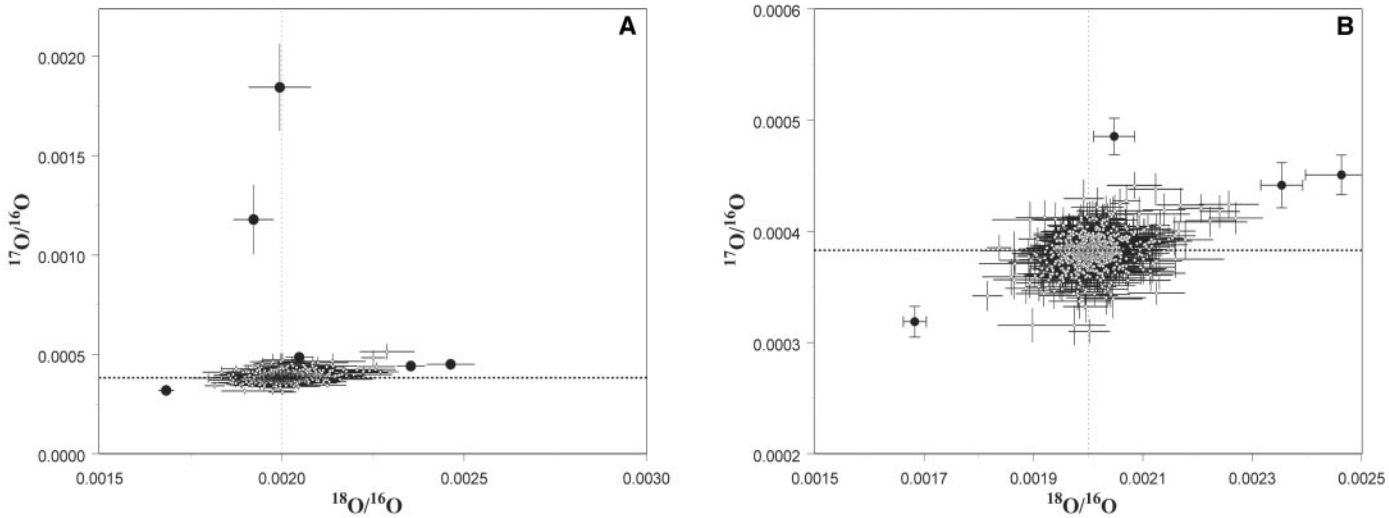


**Fig. 1.** (**A**) Oxygen isotopic ratios of 1031 subgrains determined from 25 ion images of nine cluster IDPs with 1σ errors. The identified presolar silicates are solid circles. The adjacent plot (**B**) shows the O isotopic ratios of the 750 grains with the lowest errors (1σ $\delta^{17}O$ < 50‰) on a reduced scale.

the mass, age, and chemical composition of the parent stars. Three of the silicates have O isotopic ratios characteristic of group 1 grains, which exhibit large $^{17}O$ excesses and solar $^{18}O/^{16}O$ ratios to moderate $^{18}O$ depletions, similar to those observed in red giant (RG) and asymptotic giant branch (AGB) stars. The isotopic compositions of grains formed from RG and AGB stars are influenced by deep convection in the stellar interiors, which mixes the ashes of H burning in the CNO cycle into the stellar envelopes. This occurs as main sequence stars evolve onto the RG branch (the first dredge-up), when significant mass loss begins. The variations in the $^{17}O/^{16}O$ ratios of group 1 grains are a function of the masses of the parent stars, which determine the depth of the convective envelope. A second dredge-up occurs for stars >4 solar masses after the end of He burning, as stars ascend the AGB, also affecting the surface O isotopic composition. The low $^{18}O/^{16}O$ ratios of group 2 grains have been ascribed to transport of material from H-burning regions to the base of the convective envelope in low-mass stars [cool bottom processing (*25*)]. So far, no silicates and few spinels are observed with such compositions. One silicate was found to be $^{16}O$-rich and thus falls into group 3. These grains are considered to originate from low-metallicity RG and AGB stars after the first and second dredge-ups. The two $^{17}O$- and $^{18}O$-rich silicates are enigmatic. Among circumstellar oxides, such group 4 grains are rare and have no confirmed stellar source. Possible sources include metal-rich stars and type II supernovae (*24*, *26*).

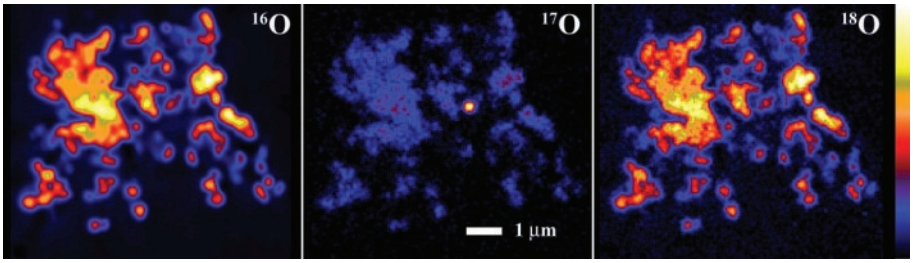


**Fig. 2.** Oxygen isotopic images of a slice of IDP L2005 C13. A presolar grain with a large $^{17}O$ excess can be clearly seen in the $^{17}O$ image.

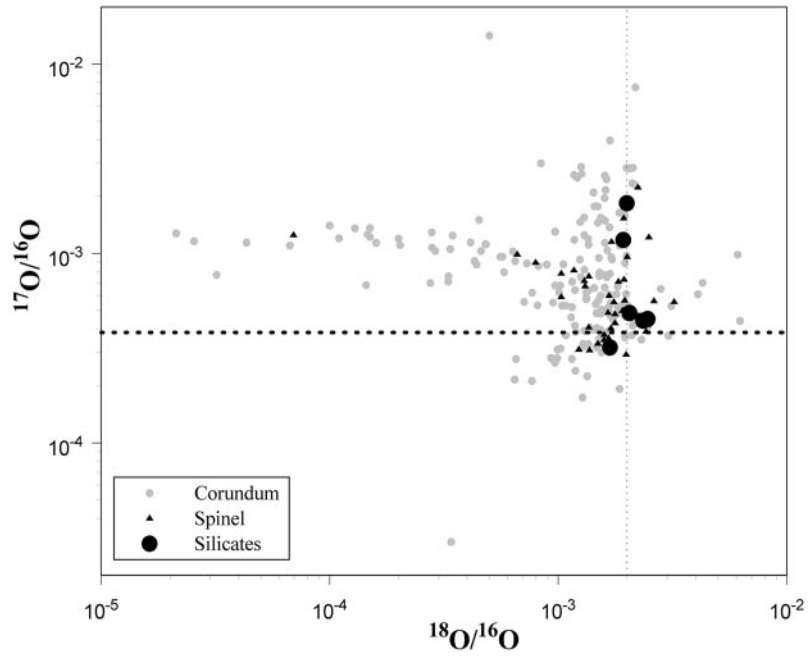


**Fig. 3.** O isotopic compositions of the circumstellar silicates of this study are compared with those previously reported for corundum (*24–26*, *38–43*) and spinel (*26*, *39*, *44*).

**Table 1.** Characteristics of interstellar silicates located in IDPs. The IDPs are named by the collector number (e.g., L2005), followed by the cluster number from that collector. n.d., not determined.

| Parent IDP | $^{17}O/^{16}O$ (1σ) | $^{18}O/^{16}O$ (1σ) | Diameter (nm) | Mineral |
|---|---|---|---|---|
| L2005 C13 | $1.84 \times 10^{-3}$ ($2.2 \times 10^{-4}$) | $1.99 \times 10^{-3}$ ($8.5 \times 10^{-5}$) | 300 | n.d. |
| L2005 C13 | $3.19 \times 10^{-4}$ ($1.4 \times 10^{-5}$) | $1.68 \times 10^{-3}$ ($2.1 \times 10^{-5}$) | 400 | GEMS |
| L2005 C13 | $4.85 \times 10^{-4}$ ($1.6 \times 10^{-5}$) | $2.05 \times 10^{-3}$ ($3.7 \times 10^{-5}$) | 330 | Forsterite |
| L2036 C4 | $4.50 \times 10^{-4}$ ($1.8 \times 10^{-5}$) | $2.46 \times 10^{-3}$ ($6.6 \times 10^{-5}$) | 940 | n.d. |
| L2036 C4 | $4.41 \times 10^{-4}$ ($2.0 \times 10^{-5}$) | $2.35 \times 10^{-3}$ ($3.8 \times 10^{-5}$) | 630 | GEMS |
| L2036 C4 | $1.18 \times 10^{-3}$ ($1.7 \times 10^{-4}$) | $1.92 \times 10^{-3}$ ($5.5 \times 10^{-5}$) | 300 | n.d. |

**Characteristics of circumstellar grains.** To gain a clearer view of the characteristics and petrographic context of circumstellar silicates, we mapped in detail all crystalline and amorphous grains (>200 nm) in six microtome thin sections by TEM before isotopic analysis (*27*). Roughly 113 of these grains were measured with sufficient precision to distinguish solar system material from circumstellar dust [1σ $\delta^{17}O/^{16}O <$ 75 per mil (‰), 1σ $\delta^{18}O/^{16}O <$ 50‰ (*28*, *29*)]. These grains include 36 enstatites, 42 GEMS (glass with embedded metal and sulfides) (*11*, *13*), 23 olivines (60 to 100 mol. % $Mg_2SiO_4$), 5 anorthites, 3 Ca,Al,Mg-rich glassy grains, 2 low-Ca pyroxene grains, and 1 grain each of diopside and chromite. Two of these grains were circumstellar in origin: A (group 1) 300-nm forsterite grain and a (group 3) 400-nm GEMS grain. Both grains were found in the same slice, and a $^{17}O$-rich grain ($^{17}O/^{16}O \sim 5 \times$ solar) of undetermined mineralogy appeared in another slice of this IDP (L2005 C13). In one case, we determined the mineralogy of a presolar grain (also a GEMS grain) after NanoSIMS analysis (*20*). Here we were able to confirm the unusual isotopic composition of the grain ($^{16}O$-poor) after transferring the section back to an Au substrate for a second NanoSIMS analysis. The petrographic settings of the circumstellar grains identified in TEM slices are not distinct from the other (solar) components in the IDPs, because they occur isolated in the carbonaceous matrix that binds minerals in the IDPs. Unfortunately, the circumstellar forsterite appears to have been thermally modified during atmospheric entry heating, making it impossible to determine whether there is microstructural evidence of its exposure in the interstellar medium (ISM) such as a high track density or a radiation-damaged rim.

Previous chemical and mineralogical studies of GEMS have found intriguing similarities to the properties of common interstellar silicates inferred from spectroscopy (*13*). Here we have identified at least two GEMS whose O isotopic compositions establish their circumstellar origins. However, the other 40 GEMS analyzed have solar isotopic compositions, and thus it is impossible to decide whether they are solar system materials or interstellar grains whose O isotopic compositions have been equilibrated. It is possible that GEMS represent a common end product of a universal process that occurs in the ISM and around newly formed stars. In this case,

most of the crystalline silicates and GEMS in IDPs are of solar system origin, variably mixed with a minor population of circumstellar grains.

**Sources of circumstellar grains.** Spectroscopic observations of RG and AGB dust shells acquired with the Infrared Space Observatory have unveiled a rich distribution of emission features attributed to amorphous silicates, enstatite, and forsterite (*30*, *31*). Thus, the identification of circumstellar forsterite and GEMS grains is consistent with these observations. Though the relative abundances of these components are sensitive to the stellar environment (*32*), amorphous grains are usually the most abundant. However, crystalline silicates are not detected in the ISM, and upper limits on their abundance range from 2 to 5% (*33*, *34*). This suggests that crystalline silicates are commonly destroyed or rendered amorphous by shocks and high-energy radiation in the ISM. It is possible that only those crystalline circumstellar silicates with short interstellar residence times or those that have been protected with coatings will be found in IDPs.

Although it has been proposed that isotopically solar GEMS are formed in the ISM by reaccretion of sputtered material (*13*), it is not possible to form high-temperature minerals such as enstatite and forsterite under these conditions. Further, it is rare for evolved stars to form stardust with solar isotopic ratios. Consequently, our observations do not support the idea that IDPs are pristine aggregates of interstellar grains. Instead, the IDPs we studied are primarily composed of materials formed at high temperatures in the protosolar nebula [perhaps by nebular shocks (*35*) or transported from the inner (warmer) regions of the solar nebula (*36*)] and variable proportions of preserved stardust and molecular cloud material.

We estimate a preliminary average abundance of silicate stardust in IDPs to be ~5500 parts per million (ppm) by taking the ratio of the total area of the circumstellar grains (~1.7 $\mu m^2$) to the total area imaged (308 $\mu m^2$). This value should be considered a lower limit, given that useful measurements were only achieved for grains >200 nm in size. This abundance is far in excess of the total circumstellar grain abundance in meteorites, which is less than 20 ppm [excluding nanodiamonds (*37*)]. The fact that these IDPs have such high abundances of stardust not found in meteorites, coupled with their preservation of delicate molecular cloud materials, suggests that they originated from parent bodies far more primitive than meteorites. Potential sources are short-period comets, as they are likely to harbor the least-altered remnants from the epoch of solar system formation.

### References and Notes


1. S. A. Sandford, *Fund. Cosmic Phys.* **12**, 1 (1987).
2. S. Messenger, *Meteorit. Planet. Sci.* **37**, 1491 (2002) and references therein.
3. J. P. Bradley, S. A. Sandford, R. M. Walker, in *Meteorites and the Early Solar System*, J. Kerridge, M. S. Matthews, Eds. (Univ. of Arizona Press, Tucson, AZ, 1988), pp. 861–895.
4. S. Messenger, *Nature* **404**, 968 (2000).
5. _____, R. M. Walker, in *Astrophysical Implications of the Laboratory Study of Presolar Materials*, T. J. Bernatowicz, E. Zinner, Eds. (American Institute of Physics, Woodbury, NY, 1998), pp. 545–564.
6. These grains are identified as "circumstellar" or equivalently "stardust," because their O isotopic compositions establish their origins as stellar ejecta. These grains must also have traversed the interstellar medium before their incorporation into the nascent solar nebula, and could also be considered "interstellar dust."
7. E. Zinner, *Annu. Rev. Earth Planet. Sci.* **26**, 147 (1998).
8. S. Messenger, T. J. Bernatowicz, *Meteorit. Planet. Sci.* **35**, A109 (2000).
9. C. M. O'D. Alexander, L. R. Nittler, F. Tera, *Lunar Planet. Sci.* **32**, 2191 (2001).
10. J. P. Bradley, D. E. Brownlee, D. R. Veblen, *Nature* **310**, 473 (1983).
11. GEMS grains are a major component of cometary/anhydrous IDPs, occasionally exceeding 50 weight % of the IDP mass. They are typically 0.1 to 0.5 $\mu m$ in size, have approximately chondritic elemental abundances (with the exception of C), and have optical properties consistent with those observed for interstellar amorphous silicates (*13*). GEMS have also been observed within isotopically anomalous (H and N) organic matter thought to be of presolar origin (*12*).
12. L. P. Keller, S. Messenger, J. P. Bradley, *J. Geophys. Res.*, **105**, 10397 (2000).
13. J. P. Bradley *et al.*, *Science* **285**, 1716 (1999).
14. F. J. Stadermann, thesis, University of Heidelberg, Germany (1991).
15. K. D. McKeegan, thesis, Washington University, St. Louis, MO (1987).
16. T. M. Esat, D. E. Brownlee, D. A. Papanastassiou, G. J. Wasserburg, *Science* **206**, 190 (1979).
17. J. Bradley, T. Ireland, in *Physics, Chemistry and Dynamics of Interplanetary Dust*, B. A. S. Gustafson, M. S. Hanner, Eds. (Astronomical Society of the Pacific, Provo, UT, 1996), pp. 275–282.
18. C. Engrand, K. D. McKeegan, L. A. Leshin, J. P. Bradley, D. E. Brownlee, *Lunar Planet. Sci.* **30**, A1690 (1999).
19. The IDPs studied here include L2005 C13, L2005 C31, L2009 C7, L2009 C10, L2011 C11, L2036 C2, L2036 C3, L2036 C4, and L2036 C9. The nomenclature refers to the large area collector number (e.g., L2005), followed by the cluster IDP number (e.g., C13 = cluster 13). In most cases, the images were acquired by rastering a ~2-pA 16-KeV $Cs^+$ primary ion beam over areas ~10 × 10 $\mu m$, while simultaneously acquiring $^{16,17,18}O^-$, $^{28}Si^-$, and $^{24}Mg^{16}O^-$ secondary ion counts with five electron multipliers. Multiple (5 to 20) image scans were acquired for each sample in order to provide verification of any apparent anomalies. High-mass-resolution scans were acquired on each sample before analysis in order to ensure that the contribution of $^{16}OH^-$ to the $^{17}O^-$ peak was less than 1‰, with a mass-resolving power of at least 9000 (Cameca definition), or ~6000 in the conventional definition. Image acquisition times ranged from 3 to 10 hours, consuming 30 to 100 nm of surface material. The magnetic field was controlled with a nuclear magnetic resonance probe, which kept peak positions stable to $\Delta M/M < 5$ ppm. Thin sections were coated with 50 Å of Au or C to avoid sample charging.
20. The IDP L2036 C4 was extracted from the ion probe mount by carving a section of the Au substrate measuring 200 × 200 $\mu m$ by hand with a scalpel. The extracted section was glued to a flattened epoxy bullet with a cyanoacrylate adhesive. The Au was trimmed with a glass knife on an ultramicrotome, leaving a 30-$\mu m$ plateau containing the IDP. The IDP was then embedded in resin, and after curing several days was sliced with a diamond knife into 50-nm sections. The sections were transferred to a 1-mm-aperture grid coated with Formvar. After TEM analysis, the entire mount (Formvar with seven sections) was transferred to a preformed Au plateau, where the sections were subsequently imaged in the NanoSIMS.
21. The data were analyzed with custom software written in the Interactive Data Language. In most cases, a range of image layers (5 to 10) was selected, discarding the first low-intensity images and the final images, which for the TEM sections were often compromised by rapid erosion of the epoxy or carbon substrate. Candidate grains were manually defined and semiautomatically redefined in subsequent layers, with the particle positions and outlines being checked in each image layer.
22. K. D. McKeegan, *Science* **237**, 1468 (1987).
23. In similar measurements of solar materials ($\mu m$-sized Burma spinel grains, enstatite grains, and Murchison matrix), we have found that in some cases the instrumental mass discrimination is sensitive to the sample stage position for given tuning conditions. However, within a small field of view (20 $\mu m$), the variations in the measured isotopic compositions of standard materials are not substantially greater than is expected from counting error. The data were corrected for discrimination (which is dominated by the varying sensitivities of the detectors) layer by layer for each subgrain, taking the weighted mean oxygen isotopic ratios of the subgrains as the solar values ($^{16}O/^{17}O = 2610$, $^{16}O/^{18}O = 498.7$). The standard deviations of the isotopic compositions of these "standard subgrains" were taken into account in the determination of the final measurement uncertainty. Final isotopic ratios and uncertainties were determined according to standard procedures. Grains that have O isotopic compositions that deviate from solar compositions by at least 3$\sigma$ are identified as stardust.
24. L. R. Nittler, C. M. O'D. Alexander, X. Gao, R. M. Walker, E. Zinner, *Astrophys. J.* **483**, 475 (1997).
25. G. J. Wasserburg, A. I. Boothroyd, I.-J. Sackmann, *Astrophys. J.* **447**, L37 (1995).
26. B.-G. Choi, G. R. Huss, G. J. Wasserburg, R. Gallino, *Science* **282**, 1284 (1998).
27. We used a JEOL 2000FX TEM equipped with an Oxford instruments energy-dispersive x-ray (EDX) spectrometer to analyze ultramicrotome thin sections of the IDPs. The mineralogy and composition of grains >200 nm in diameter were determined with a combination of electron diffraction and quantitative EDX analysis and dark-field imaging.
28. Delta values represent the deviation of the measured isotopic ratio ($R_{measured}$) from the value of the terrestrial standard ($R_{standard}$), in parts per thousand (‰): $\delta R = (R_{measured}/R_{standard} - 1) \times 1000$.
29. Of the 50 subgrains with the smallest measurement errors ($1\sigma\ \delta^{17}O < 40$‰, $1\sigma\ \delta^{18}O < 20$‰), 49 have solar O isotopic ratios within 2$\sigma$, and one is a circumstellar grain. We achieved the highest precision isotopic measurements on ultramicrotome thin sections deposited onto Au substrates. This mounting technique offers very flat conducting samples. Images acquired from TEM grid sections were limited by the sputtering lifetime of the epoxy and were compromised by stretching and tearing of holes in the epoxy and C substrate during the measurements.
30. L. B. F. M. Waters *et al.*, *Astron. Astrophys.* **315**, L361 (1996).
31. L. B. F. M. Waters *et al.*, in *Thermal Emission Spectroscopy and Analysis of Dust, Disks, and Regoliths*, M. L. Sitko, A. L. Sprague, D. V. Lynch, Eds. (Astronomical Society of the Pacific, San Francisco, CA, 2000), pp. 3–14.
32. F. Kemper, L. B. F. M. Waters, A. de Koter, A. G. G. M. Tielens, *Astron. Astrophys.* **369**, 132 (2001).
33. F. J. Molster, J. P. Bradley, M. L. Sitko, *Lunar Planet. Sci.* **33**, A1471 (2002).
34. A. Li, B. T. Draine, *Astrophys. J.* **550**, L213 (2001).
35. D. E. Harker, S. J. Desch, *Astrophys. J.* **565**, L109 (2002).
36. D. Bocklée-Morvan, D. Gautier, F. Hersant, J.-M. Huré, F. Robert, *Astron. Astrophys.* **384**, 1107 (2002).
37. Although the nanodiamonds are abundant in meteorites (up to 1000 ppm), it is possible that only a small fraction are presolar in origin, because the bulk

C isotopic composition is solar and the anomalous Xe and N have low abundances.
38. B.-G. Choi, G. J. Wasserburg, G. R. Huss, *Astrophys. J.* **522**, L133 (1999).
39. L.R. Nittler *et al.*, *Lunar Planet. Sci.* **34**, Abstract 1703 (2003).
40. G. Huss, A. J. Fahey, R. Gallino, G. J. Wasserburg, *Astrophys. J.* **430**, L81 (1994)
41. I. D. Hutcheon, G. R. Huss, A. J. Fahey, G. J. Wasserburg, *Astrophys. J.* **425**, L97 (1994).
42. N. Krestina, W. Hsu, G. J. Wasserburg, *Lunar Planet. Sci.* **33**, A1425 (2002).
43. L. R. Nittler, C. M. O'D. Alexander, J. Wang, X. Gao, *Nature* **393**, 222 (1998).
44. E. Zinner *et al.*, in preparation.
45. Supported by NASA grants NAG5-9801 and RTOP 344-31-40-07. This work was enabled by the revolutionary NanoSIMS ion microprobe, which was designed by G. Slodzian at the University of Orsay, Paris.

18 November 2002; accepted 19 February 2003
Published online 27 February 2003;
10.1126/science.1080576
Include this information when citing this paper.

# Gating the Selectivity Filter in ClC Chloride Channels

**Raimund Dutzler, Ernest B. Campbell, Roderick MacKinnon***

**ClC channels conduct chloride ($Cl^-$) ions across cell membranes and thereby govern the electrical activity of muscle cells and certain neurons, the transport of fluid and electrolytes across epithelia, and the acidification of intracellular vesicles. The structural basis of ClC channel gating was studied. Crystal structures of wild-type and mutant *Escherichia coli* ClC channels bound to a monoclonal Fab fragment reveal three $Cl^-$ binding sites within the 15-angstrom neck of an hourglass-shaped pore. The $Cl^-$ binding site nearest the extracellular solution can be occupied either by a $Cl^-$ ion or by a glutamate carboxyl group. Mutations of this glutamate residue in *Torpedo* ray ClC channels alter gating in electrophysiological assays. These findings reveal a form of gating in which the glutamate carboxyl group closes the pore by mimicking a $Cl^-$ ion.**

Ion channels carry electric current across the membrane of cells in the form of diffusing ions. The two key properties of ion channels are selective ion conduction and gating. Selective conduction refers to a channel's ability to select one ionic species among those present in the cellular environment and catalyze its rapid flow through the pore; gating refers to opening and closing the pore, the process by which ion conduction is turned on or off.

In some channels, the functions of selective conduction and gating are mediated by quite separate structural elements. Potassium channels, for example, have a selectivity filter near the extracellular side of the pore and a gate near the intracellular side (*1*). Separation of the filter and gate allows ligand-binding domains or voltage sensor domains to open and close the pore through large conformational changes without affecting the selectivity filter, whose structure must be maintained in order to discriminate among ions on the basis of their small differences in radius (*2*–*4*).

Years of electrophysiological study suggest that the condition of a structurally independent selectivity filter and gate will probably not apply to ClC channels, a large $Cl^-$ channel family whose members are found from bacteria to animals (*5*–*7*). In ClC channels, selective conduction and a certain form of gating referred to as "fast gating" seem to be intimately coupled to each other. Chloride ions conduct rapidly through the pore, and at the same time they affect the probability that the fast gate will be open (*8, 9*). Certain ClC channels have even been called "$Cl^-$-activated $Cl^-$ channels" because extracellular $Cl^-$ causes the gate to open (*8, 9*). Membrane voltage can influence the open probability as well, but even this property depends on $Cl^-$ ions (*8, 9*).

We sought to understand the structural origins of gating in ClC channels and why gating is closely tied to $Cl^-$ ion conduction. Specifically, we tested a possibility raised by the first ClC channel structures: that a glutamate side-chain carboxyl group gates the pore by binding to a $Cl^-$ ion site within the selectivity filter (*10*).

**Structure of a ClC channel bound to a Fab.** A reasonably high-resolution structure was required in order to define the $Cl^-$ ion coordination chemistry within the conduction pore with accuracy. To this end, monoclonal antibodies were raised and a crystal structure of an *E. coli* ClC channel bound to a Fab fragment was determined at 2.5 Å resolution (*11*) (Table 1). A single Fab was attached to the extracellular

Howard Hughes Medical Institute, Laboratory of Molecular Neurobiology and Biophysics, Rockefeller University, 1230 York Avenue, New York, NY 10021, USA.

*To whom correspondence should be addressed. E-mail: mackinn@rockvax.rockefeller.edu

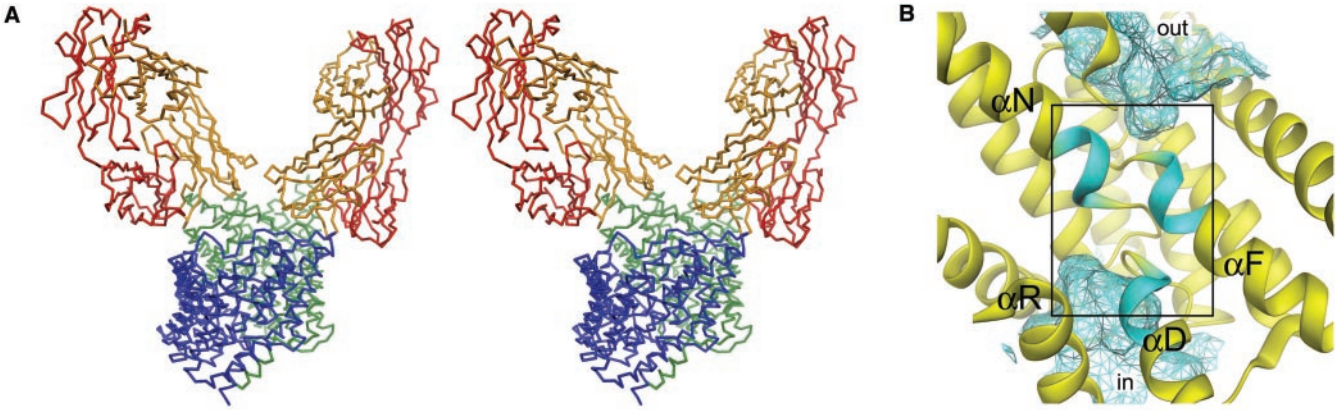


**Fig. 1.** Structure of the EcClC Fab complex. (**A**) Stereo view of a Cα representation of the EcClC channel in complex with two Fab fragments. The complex is viewed at an angle of about 30° from the plane of the membrane. The two ClC subunits are colored blue and green; the light and heavy chains of the two Fab fragments are colored red and orange, respectively. (**B**) View of the ion-conducting pore of the ClC subunit. The pore is viewed from the dimer interface, with foreground α helices removed for clarity. The protein is shown as a ribbon. The N-terminal ends of α helices D, F, and N are cyan. Aqueous cavities from the extracellular solution (out) and intracellular solution (in) are shown as cyan mesh. The selectivity filter is indicated by a black frame. Figures 1, 2, and 4 were prepared with DINO (www.dino3d.org).